Assessing CFD Modeling of Entropy Generation for the Air Frame Subsystem in an Integrated Aircraft Design/Synthesis Procedure

Kehinde Alabi[*], Foluso Ladeinde.[†]
Thaerocomp Technical Corp., P. O. Box 1527, Stony Brook, NY, 11790-0609

Mike vonSpakovsky[‡]
Department of Mechanical Engineering, VPI, Blacksburg, VA, 24061-0238

and

David Moorhouse[§], Jose Camberos[**]
AFRL/VASD, Wright-Patterson Air Force Base, Dayton, OH 45433-7542

This paper presents the CFD modeling of entropy generation of the Air Frame Subsystem as a component of integrated aircraft design/synthesis. Entropy calculation procedures for complicated geometries in curvilinear coordinates are described, including the effects of turbulence. Both inviscid and viscous calculations are reported and the contributions of the various terms in the entropy equation are investigated. The procedure is validated and then extended to the calculation of entropy generation associated with flow over the B747-200 aircraft. Results show that most of the entropy generation is due to turbulence. The viscous dissipation term in the entropy equation dominates compared to the heat transfer term. The implications of the results for design improvement are briefly discussed.

Nomenclature

C_p	=	pressure coefficient
f	=	friction factor
M_∞	=	free stream Mach number
J	=	Jacobian of the coordinate transformation matrix
k	=	turbulence kinetic energy
Pr_T	=	turbulence Prandtl number
s	=	entropy generation
S_{ij}	=	"*ij*" component of the strain rate tensor
$\dot{S}_{gen}$	=	entropy generation rate per unit volume
T_w	=	wall temperature
γ	=	ratio of specific heats
t	=	time
u, v, w	=	velocity components in the *x, y, z* Cartesian coordinate directions, respectively
u_τ	=	friction velocity

---

[*] Research Engineer, Ph.D, AIAA Member.
[†] Director of Research, AIAA Life Member & Associate Fellow.
[‡] Professor & Director for Center for Energy Systems Research, AIAA Member.
[§] Director, Multidisciplinary Technologies Center, AIAA Associate Fellow.
[**] Aerospace Engineer, AIAA Associate Fellow.

American Institute of Aeronautics and Astronautics

(x, y, z)	=	the Cartesian coordinate directions
y^+	=	shortest distance to the nearest wall normalized by the friction velocity and fluid kinematic viscosity
α	=	angle of attack
μ_T, ν_T	=	turbulence dynamic and kinematic viscosities, respectively
ρ	=	fluid density
ε	=	turbulence kinetic energy dissipation rate
τ_{ij}	=	the "ij" component of the shear stress tensor
(ξ, η, ζ)	=	the curvilinear coordinate directions

I.   Introduction

The design/optimization of a complete aircraft system is difficult to analyze as one problem. The reasons for this include the high computational requirement and the disparate disciplines and/or location of personnel required for the various subsystems.[1] The resolution of this difficulty has led to various decomposition procedures.[2,3] Of interest in the present paper is the potential role of CFD as a component of an overall procedure for integrated design/synthesis of aerospace systems.

A complete aircraft design problem typically consists of many subsystems, including the Air Frame-Structural, Air Frame-Aerodynamics, Environmental Control, Propulsion, Vapor Compression / PAO Loops Subsystem, Electrical, Hydraulic, Fuel Loop, Expendable Payload, Equipment Group, Permanent Payload, and Controls. In the present paper, the Air Frame Subsystem – Aerodynamics (AFS-A) is addressed via the use of advanced CFD software called AEROFLO developed by Thaerocomp Technical Corp. (TTC)for multi-disciplinary simulation. In particular, the contribution of this subsystem to the overall entropy generation in a complete aircraft design/synthesis task is investigated.

Exergy or energy availability and entropy-based methods are gaining increased use in system synthesis and design. Compared to energy-based formulation which deals with the conversion and conservation of energy, entropy-based analysis additionally provides information on the quality of energy or the energy that is available for useful work. Adeyinka & Naterer[4] presented CFD calculations of loss analysis based on entropy generation rate that is consistent with traditional energy-based loss correlations and used the procedure to select optimal diffuser geometry for the least losses. Sciubba[5] used local entropy generation results to suggest areas for improvement in turbomachinery designs. Adeyinka & Naterer[6] showed that the flow losses in pipes could be directly measured by the entropy generation rate. A detailed review of entropy and its significance in CFD is presented by Naterer and Camberos.[7]

In spite of the foregoing, entropy-based simulations provide a challenge because of the scarcity of experimental data to validate computations.[6] As a result, many entropy-based studies have relied on analytic solutions for validation, using simple canonical problems. To our knowledge, entropy-based procedures have not yet been applied to entire aircraft geometry. An objective of the current work is to demonstrate the viability of entropy-based methods for more geometrically complicated fluid dynamic problems. It is pointed out that a representation of losses in terms of entropy generation offers significant insight into the flow and thermal transport phenomena over the air frame and provides an effective tool for improving performance. For AFS-A, the general areas for design improvement could include the shape of the wing, the construction details of the leading and trailing edges, the fuselage, and the various appendages. After the flow and thermal fields have been computed, the local values of the thermal and entropy-generation rates can be obtained. The information enables the designer to detect, by inspection, the key areas that require a modification in order to obtain an optimized design. The platform for the present analysis is the Boeing 747-200 commercial aircraft. Entropy generation from both inviscid and viscous calculations is reported. The integration of the CFD-generated data for AFS-A into the overall design/synthesis for a complete aircraft is the motivating factor for the present work.

II. The CFD Procedure for Entropy Generation

The flows of interest are turbulent which, combined with the complex geometries involved, tests the ability of any CFD tool to generate accurate design data. At a first glance, it would seem that accurate entropy generation data could be obtained by solving the evolution equation for the entropy per unit volume:

$$\partial_t \rho s + \partial_j \rho u_j s + \partial_j \frac{q_j}{T} = -\frac{q_j \partial_j T}{T^2} + \frac{\tau_{ij} \partial_j u_i}{T}. \tag{1}$$

If we assume RANS-type averaging for a moment: $u_i = \bar{u}_i + u_i'$, where $\bar{u}_i$ is the average velocity and u_i' is the fluctuating velocity, we end up with the following equation for averaged entropy:[8]

$$\bar{\rho}\overline{\partial_t s} + \partial_i \left(\overline{\rho s}\,\bar{u}_i + \bar{\rho}\overline{s' u'}_i + \bar{s}\overline{\rho' u'}_i + \bar{u}_i \overline{\rho' s'} + \overline{\rho' s' u'}_i - k \overline{\ln\left[\bar{T}\left(1 + \frac{T'}{\bar{\bar{T}}}\right)\right]} \right)$$

$$= k \partial_i \ln \bar{T} \partial_i \ln \bar{T} + k \overline{\partial_i (\ln T)' \partial_i (\ln T)'} + \mu\left(\left(\overline{\frac{1}{T}}\right)\partial_j \bar{u}_i \partial_j \bar{u}_i + \left(\overline{\frac{1}{T}}\right)\overline{\partial_j u'_i \, \partial_j u'_i} \right.$$

$$+ 2\partial_j \bar{u}_i \overline{\left(\frac{1}{T}\right)' \partial_j u'_i} + \overline{\left(\frac{1}{T}\right)' \partial_j u'_i \, \partial_j u'_i} + \left(\overline{\frac{1}{T}}\right)\partial_j \bar{u}_i \partial_i \bar{u}_j + \left(\overline{\frac{1}{T}}\right)\overline{\partial_j u'_i \, \partial_i u'_j} + \partial_j \bar{u}_i \overline{\left(\frac{1}{T}\right)' \partial_i u'_j} + \partial_i \bar{u}_j \overline{\left(\frac{1}{T}\right)' \partial_j u'_i}$$

$$+ \overline{\left(\frac{1}{T}\right)' \partial_j u'_i \, \partial_i u'_j} - \frac{2}{3}\left(\left(\overline{\frac{1}{T}}\right)\partial_i \bar{u}_i \partial_k \bar{u}_k + \left(\overline{\frac{1}{T}}\right)\overline{\partial_i u'_i \, \partial_k u'_k} + 2\partial_i \bar{u}_i \overline{\left(\frac{1}{T}\right)' \partial_k u'_k} + \overline{\left(\frac{1}{T}\right)' \partial_i u'_i \, \partial_k u'_k} \right) \right).$$

The terms $\left(\frac{1}{T}\right)'$ and $\overline{\left(\frac{1}{T}\right)}$ need to be modeled in the foregoing equations, with the understanding that $\frac{1}{\bar{T}} \neq \overline{\left(\frac{1}{T}\right)}$.

Entropy generation obtained from the solution of the entropy transport equation will probably not be accurate. Instead, formulations based on the Onsager relations[9] are preferred in order to avoid unphysical results. This relation is quasi-steady:

$$\dot{S}_{gen} = \frac{1}{T}\tau_{ij}\frac{\partial u_i}{\partial x_j} - \frac{q_k}{T^2}\frac{\partial T}{\partial x_k}, \tag{2}$$

where the term on the left-hand side represents the entropy generation per unit volume. The first term on the right represents irreversibilities related to the degradation of mechanical energy into internal energy[6] while the second term represents irreversiblities related to heat transfer across finite temperature differences.

Although Eq. (2) appears to be more convenient for calculating entropy generation compared to the transport equation, it shares some of the turbulence modeling problems associated with the viscous dissipation and heat flux-temperature gradient correlation, which can be written as $\overline{\frac{1}{T}\tau_{ij}\partial_j u_i}$ and $\overline{\left(\frac{-q_i \partial_i T}{T^2}\right)}$, respectively. Note that these terms can be expanded as follows:

$$\overline{\frac{1}{T}\tau_{ij}\partial_j u_i} = \mu\overline{\left(\frac{1}{2}\left(\frac{1}{T}\partial_j u_i^2 + 2\frac{1}{T}\partial_i u_j \partial_j u_i + \frac{1}{T}\partial_i u_j^2 \right) - \frac{2}{3}\frac{1}{T}\partial_i u_i \partial_k u_k \right)}$$

$$= \mu\left[\left(\overline{\frac{1}{T}}\right)\partial_j \bar{u}_i \partial_j \bar{u}_i + \left(\overline{\frac{1}{T}}\right)\overline{\partial_j u'_i \, \partial_j u'_i} + 2\partial_j \bar{u}_i \overline{\left(\frac{1}{T}\right)' \partial_j u'_i} \right.$$

$$\left. + \overline{\left(\frac{1}{T}\right)' \partial_j u'_i \, \partial_j u'_i} + \left(\overline{\frac{1}{T}}\right)\partial_j \bar{u}_i \partial_i \bar{u}_j + \left(\overline{\frac{1}{T}}\right)\overline{\partial_j u'_i \, \partial_i u'_j} \right.$$

$$+ \overline{\partial_j \bar{u}_i \left(\frac{1}{T}\right)' \partial_i u'_j} + \overline{\partial_i \bar{u}_j \left(\frac{1}{T}\right)' \partial_j u'_i} + \overline{\left(\frac{1}{T}\right)' \partial_j u'_i \partial_i u'_j}$$

$$- \frac{2}{3}\left[\overline{\left(\frac{1}{T}\right)} \partial_i \bar{u}_i \partial_k \bar{u}_k + \overline{\left(\frac{1}{T}\right)} \partial_i u'_i \partial_k u'_k + 2\partial_i \bar{u}_i \overline{\left(\frac{1}{T}\right)' \partial_k u'_k} + \overline{\left(\frac{1}{T}\right)' \partial_i u'_i \partial_k u'_k}\right]\Bigg]\Bigg],$$

and

$$\overline{\left(\frac{-q_i \partial_i T}{T^2}\right)} = \overline{k \partial_i \ln T \partial_i \ln T} \quad = k \overline{\partial_i \ln T} \overline{\partial_i \ln T} + k \overline{\partial_i (\ln T)' \partial_i (\ln T)'}.$$

We see that the terms on the right-hand side need to be modeled.

The foregoing modeling issues are topical and have not received enough attention. The invocation of the so-called "Small Thermal Turbulence Assumption" proposed by Bevan-Kramer[8] allowed some calculations but the basic modeling issues remain. Adeyinka and Naterer[6] provided a deeper insight into the problem in a recent paper.

For the present studies, we have used the model proposed by Moore[10] to calculate the average entropy generation per unit volume:

$$\bar{S}_{gen} = \frac{1}{\bar{T}} \bar{\tau}_{ij} \frac{\partial \bar{u}_i}{\partial x_j} - \frac{\bar{q}_k}{\bar{T}^2} \frac{\partial \bar{T}}{\partial x_k}, \tag{3}$$

where eddy viscosity-type assumptions are made:

$$\bar{\tau}_{ij} = (\mu + \mu_T)\left(\frac{\partial \bar{u}_i}{\partial x_j} + \frac{\partial \bar{u}_j}{\partial x_i} - \frac{2}{3}\frac{\partial \bar{u}_k}{\partial x_k}\delta_{ij}\right),$$

and

$$\bar{q}_k = -\left(\frac{\mu}{Pr} + \frac{\mu_T}{Pr_T}\right)\frac{\partial \bar{T}}{\partial x_k}.$$

The average entropy generation rate can be expressed in non-dimensional form as follows:

$$\bar{\bar{S}}_{gen} = \frac{1}{Re}\frac{\mu + \mu_T}{\bar{T}}\left\{2\left(\frac{\partial \bar{u}}{\partial x}\right)^2 + 2\left(\frac{\partial \bar{v}}{\partial y}\right)^2 + 2\left(\frac{\partial \bar{w}}{\partial z}\right)^2 - \frac{2}{3}\left(\frac{\partial \bar{u}}{\partial x} + \frac{\partial \bar{v}}{\partial y} + \frac{\partial \bar{w}}{\partial z}\right)^2 + \right.$$

$$\left. \left(\frac{\partial \bar{u}}{\partial y} + \frac{\partial \bar{v}}{\partial x}\right)^2 + \left(\frac{\partial \bar{u}}{\partial z} + \frac{\partial \bar{w}}{\partial x}\right)^2 + \left(\frac{\partial \bar{w}}{\partial y} + \frac{\partial \bar{v}}{\partial z}\right)^2\right\}$$

$$+ \frac{1}{(\gamma - 1)M_\infty^2 Re Pr}\frac{\mu/Pr + \mu_T/Pr_T}{\bar{T}^2}\left\{\left(\frac{\partial \bar{T}}{\partial x}\right)^2 + \left(\frac{\partial \bar{T}}{\partial y}\right)^2 + \left(\frac{\partial \bar{T}}{\partial z}\right)^2\right\}, \tag{4}$$

where, for the curvilinear coordinate system used, we have

$$\frac{\partial u_i}{\partial x_j} = \frac{\partial u_i}{\partial \xi}\xi_{x_j} + \frac{\partial u_i}{\partial \eta}\eta_{x_j} + \frac{\partial u_i}{\partial \varsigma}\varsigma_{x_j},$$

$$\frac{\partial T}{\partial x_j} = \frac{\partial T}{\partial \xi}\xi_{x_j} + \frac{\partial T}{\partial \eta}\eta_{x_j} + \frac{\partial T}{\partial \varsigma}\varsigma_{x_j}.$$

Note that integration over volume of the entropy per unit volume is required in order to obtain the total entropy generation in the domain. Also note that the above formulation allows the rate of entropy generation to be computed as a derived (post-processed) quantity.

Observations have shown that the contributions to the entropy generation rate in Eq. (3) show very steep gradients close to a wall and numerical simulations are far more effective with wall functions for the production terms.[6,11,12] This is particularly important for simulations with large values of y^+ (necessary when it is

computationally impractical to resolve the flow at the wall for large calculations). The high Reynolds number k–ε model employs wall functions in place of fine resolutions at the wall. It has been used for turbulent entropy calculations.[12] The details of the model are presented below.

A. Turbulence Viscosity Models

The turbulent shear stress is approximated in the usual eddy viscosity form:

$$\widetilde{\tau}'_{ij} = 2\widetilde{\mu}_T \left[\widetilde{S}_{ij} - \frac{1}{3}\frac{\partial \widetilde{u}_k}{\partial x_k}\delta_{ij} \right] - \frac{2}{3}\widetilde{\rho}k\delta_{ij},$$

where $\widetilde{S}_{ij} = \frac{1}{2}\left(\frac{\partial \widetilde{u}_i}{\partial x_j} + \frac{\partial \widetilde{u}_j}{\partial x_i} \right)$ is the mean strain rate, $k = \frac{1}{2}\left(u'^2 + v'^2 + w'^2 \right)$ is the turbulent kinetic energy,

$\mu_t = C_\mu f_\mu \dfrac{\rho k^2}{\varepsilon}$ is the eddy viscosity, and ε is the dissipation rate of k. The following equations are solved for k and ε:

$$\frac{\partial k}{\partial t} + \widetilde{u}_j \frac{\partial k}{\partial x_j} - \frac{1}{\rho}\frac{\partial}{\partial x_j}\left(\left(\widetilde{\mu} + \frac{\widetilde{\mu}_t}{\rho_k} \right)\frac{\partial k}{\partial x_j} \right) = P - \varepsilon$$

$$\frac{\partial \varepsilon}{\partial t} + \widetilde{u}_j \frac{\partial \varepsilon}{\partial x_j} - \frac{1}{\rho}\frac{\partial}{\partial x_j}\left(\left(\widetilde{\mu} + \frac{\widetilde{\mu}_t}{\rho_\varepsilon} \right)\frac{\partial \varepsilon}{\partial x_j} \right) = \frac{C_1}{\rho}\frac{\varepsilon}{k}P - \frac{C_2\varepsilon^2}{k}.$$

The constants in the above equations are $C_\mu = 0.09$, $\rho_\kappa = 1.0$, $\rho_\varepsilon = 1.3$, $C_1 = 1.44$, $C_2 = 1.92$ and $P = \widetilde{\tau}_{ij}\widetilde{S}_{ij}$ is the turbulent production. For boundary conditions, a two layer "law of the wall" was used to impose the k and ε values at the first point (on the wall). A wall function was also used in the viscous sublayer. Details of the formulation can be found in the work of Steffen.[17]

B. Numerical Procedures

We use a high-order, finite-difference scheme in a curvilinear coordinate system. In standard notations, the filtered equations can be written as

$$\frac{\partial \hat{U}}{\partial t} + \frac{\partial}{\partial \xi}\left(\hat{F} - \frac{1}{\mathrm{Re}}\hat{F}_v \right) + \frac{\partial}{\partial \eta}\left(\hat{G} - \frac{1}{\mathrm{Re}}\hat{G}_v \right) + \frac{\partial}{\partial \xi}\left(\hat{H} - \frac{1}{\mathrm{Re}}\hat{H}_v \right) = 0, \tag{5}$$

By using the implicit, approximately-factored finite-difference algorithm of Beam-Warming and employing a Newton-like sub-iteration, we have the following algorithm:

$$\left[J^{-1^{p+1}} + \phi^i \Delta t_s \delta_\xi \left(\frac{\partial \hat{F}^p}{\partial U} - \frac{1}{\mathrm{Re}}\frac{\partial \hat{F}^p_v}{\partial U} \right) \right] J^{p+1} \times \left[J^{-1^{p+1}} + \phi^i \Delta t_s \delta_\eta \left(\frac{\partial \hat{G}^p}{\partial U} - \frac{1}{\mathrm{Re}}\frac{\partial \hat{G}^p_v}{\partial U} \right) \right] J^{p+1} \times$$

$$\left[J^{-1^{p+1}} + \phi^i \Delta t_s \delta_\zeta \left(\frac{\partial \hat{H}^p}{\partial U} - \frac{1}{\mathrm{Re}}\frac{\partial \hat{H}^p_v}{\partial U} \right) \right]\Delta U$$

$$= -\phi^i \Delta t_s \left[J^{-1^{p+1}}\frac{(1+\phi)U^p - (1+2\phi)U^n + \phi U^{n-1}}{\Delta t} - U^p \left(\left(\frac{\xi_t}{J}\right)_\xi + \left(\frac{\eta_t}{J}\right)_\eta + \left(\frac{\zeta_t}{J}\right)_\zeta \right) \right]$$

$$-\phi^i \Delta t_s \left[\delta_\xi \left(\hat{F}^p - \frac{1}{\mathrm{Re}}\hat{F}^p_v \right) + \delta_\eta \left(\hat{G}^p - \frac{1}{\mathrm{Re}}\hat{G}^p_v \right) + \delta_\zeta \left(\hat{H}^p - \frac{1}{\mathrm{Re}}\hat{H}^p_v \right) \right],$$

where

$$\phi^i = \frac{1}{1+\phi}, \Delta U = U^{p+1} - U^p.$$

and superscripts "p" and "n" denote the sub-iteration steps and the outer-loop time steps, respectively. In the above equations, (ξ, η, ς) are the curvilinear coordinate directions and Δt_s is the time step for the sub-iterations. Either a first or second-order temporal accuracy can be specified in the above iterative procedure by selecting $\phi = 0$ or $\phi = 1/2$. For $p = 1$, $U^p = U^n$ and $U^{n+1} = U^p$ at convergence in p.

Note that the default spatial discretization procedure in AEROFLO is based on high-order differencing, while the standard, simple (low order) schemes are available as options. For the former and assuming subsonic flows, we use the compact Padé approximant method for spatial differencing. Consider the differencing of a flow variable u along the ξ direction (that is, $\partial u / \partial \xi$). The problem is to utilize the known u_i values to estimate the derivative $u' \equiv \partial u / \partial \xi|_i$ at each mesh point. In the interior, a centered formula is employed:

$$\alpha u'_{i-1} + u'_i + \alpha u'_{i+1} = b \frac{u_{i+2} - u_{i-2}}{4\Delta\xi} + a \frac{u_{i+1} - u_{i-1}}{2\Delta\xi}$$

$$(\alpha, a, b) = \begin{cases} \left(\frac{1}{4}, \frac{3}{2}, 0\right) : 3 - pt, 4th - order \\ \left(\frac{1}{3}, \frac{14}{9}, \frac{1}{9}\right) : 4 - pt, 6th - order. \end{cases}$$

For high-order differencing of flow fields with shock waves, the weighted essentially non-oscillatory (WENO) procedure is used, which can be summarized as follows, if we consider the ξ direction in Eq. (5) as an example:

$$\left.\frac{\partial \hat{F}}{\partial \xi}\right|_i = \frac{1}{\Delta\xi} \left\{ \left[\tilde{R}_{Roe} \cdot \left(\tilde{R}_{Roe}^{-1} \cdot \hat{F}\right)\right]_{i+\frac{1}{2}} - \left[\tilde{R}_{Roe} \cdot \left(\tilde{R}_{Roe}^{-1} \cdot \hat{F}\right)\right]_{i-\frac{1}{2}} \right\},$$

where $\hat{F}_{i\pm\frac{1}{2}} = \frac{1}{2}\left[\hat{F} \pm \alpha \cdot \hat{U}\right]_{i+1/2}$, $\alpha = \max_u \left|\hat{F}'(u)\right|$,

and $\hat{F}^+_{i+\frac{1}{2}} = \sum_{r=0}^{k-1} \omega_r \hat{F}^{(r)+}_{i+\frac{1}{2}}$, $\hat{F}^-_{i+\frac{1}{2}} = \sum_{r=0}^{k-1} \tilde{\omega}_r \hat{F}^{(r)-}_{c,i+\frac{1}{2}}$, $\hat{F}^{(r)}_{i+\frac{1}{2}} = \sum_{m=0}^{k-1} c_{rm} \hat{F}_{i-r+m}$,

$$\omega_r = \frac{\alpha_r}{\sum_{s=0}^{k-1} \alpha_s}, \alpha_\gamma = \frac{d_r}{(\varepsilon + \beta_r)}, \quad r = 0, ..., k-1,$$
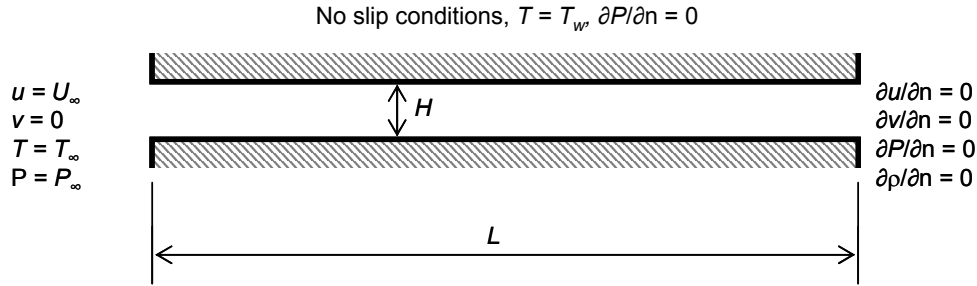
with ω_r as the normalized weights, $\overline{\omega}_r = \overline{\omega}_r(\omega_r)$ and d_γ are constants, ε is a robustness factor that prevents the occurrence of a zero denominator, while β_γ is a smoothness indicator, which is related to the undivided difference. The positive sign indicates upwind, while negative implies downwind. We set $\varepsilon \approx 10^{-14}$ and use spectral radius from coupled equation systems to compute the value of α, as opposed to a component-wise procedure to determine this parameter. Note that c_{rm} are coefficients of Lagrange interpolation formula.[13]

III.   Results

Validations of the entropy generation calculation in AEROFLO have been carried out using a laminar and turbulent channel flow, details of which are provided below.

A. Laminar Flow through a Channel

The procedures described earlier in this paper have been used to calculate the flow between two flat parallel plates, as in Erbay et. al.[14] This flow has been studied analytically and computationally by several investigators.[15,16] The physical system is illustrated in Fig. 1. The plates are separated by a distance H in the y-direction. The length of the channel, L, is $10H$ aligned parallel to the x-axis. The channel walls are both set at a temperature, $T_w = 1.1T_\infty$.

No slip conditions, $T = T_w$, $\partial P/\partial n = 0$

$u = U_\infty$
$v = 0$
$T = T_\infty$
$P = P_\infty$

H

$\partial u/\partial n = 0$
$\partial v/\partial n = 0$
$\partial P/\partial n = 0$
$\partial \rho/\partial n = 0$

L

Figure 1. Boundary conditions for flow through a channel

Since the flow equations are solved in a compressible form, the temperature values are imposed by allowing the density to vary consistently with the computed pressure to satisfy the equation of state for a perfect gas. For instance, to set T_w, the density is imposed according to the following expression:

$$\rho_w = \frac{\gamma Ma^2}{T_w}.$$

The grid used is 200 x 50 with high mesh gradients close to the wall and $y^+ = 0.064$. The Mach number and Reynolds number are 0.01 and 100, respectively. The compact schemes in AEROFLO were used for spatial differencing while the Beam-Warming scheme was used for time differencing. A time step size of 0.0005, was imposed with four sub-iterations for convergence within each time step. An initial condition of $u = 0$ and $P = 1/\gamma Ma^2$ was imposed. The simulation was run until steady state at a non-dimensional time of approximately $T = 5$.
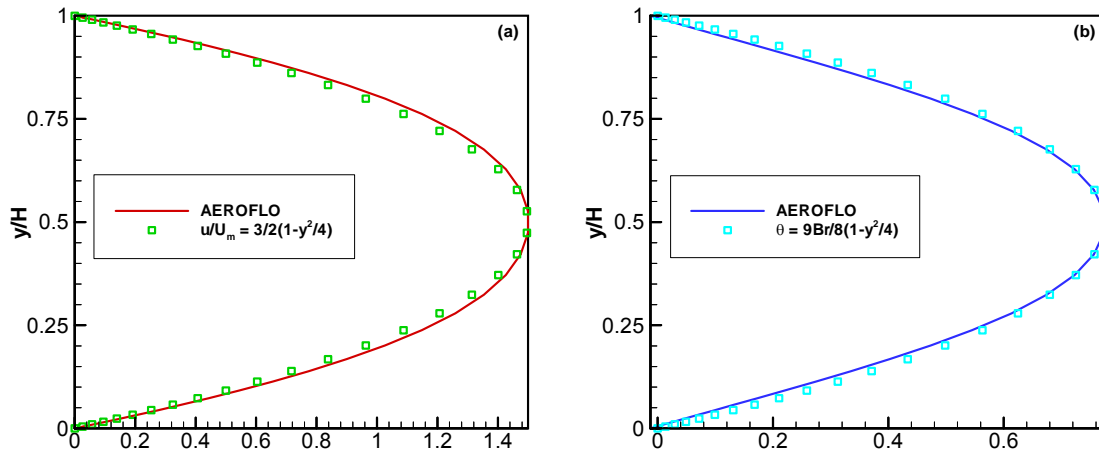
Figure 2. (a) u/U_m and (b) θ profiles compared with analytic solutions in the fully develop region.

Results are shown in Figs. 2 through 5. Figure 2 shows comparison of the flow field with analytic solutions[15] in the fully developed region at $x/H = 9$. The results show good agreement.

The average Nusselt number, Nu, at the wall was computed as 7.14 compared with the analytic value[15] of 7.534. This quantity is defined by the following expression:

$$Nu = \frac{q''}{T_w - T_\infty} = \frac{-\left.\dfrac{\partial T}{\partial y}\right|_{y=wall}}{T_w - 1}.$$

Figure 3 shows the Nusselt number profile at the wall for the current calculations compared with the calculations of Erbay et. al.[14] The results show good agreement except close to the inlet region. Note that in order to satisfy the equation of state, the density at the walls has a value of 1/1.1.
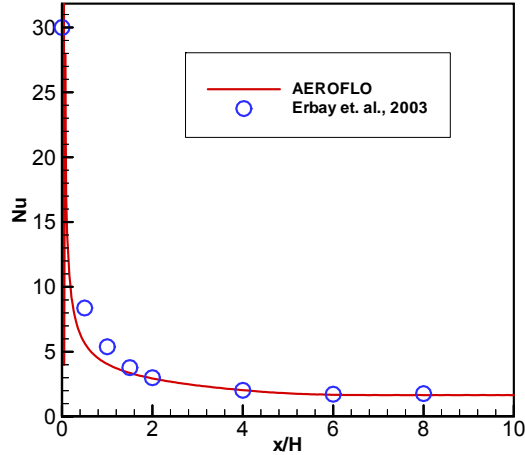
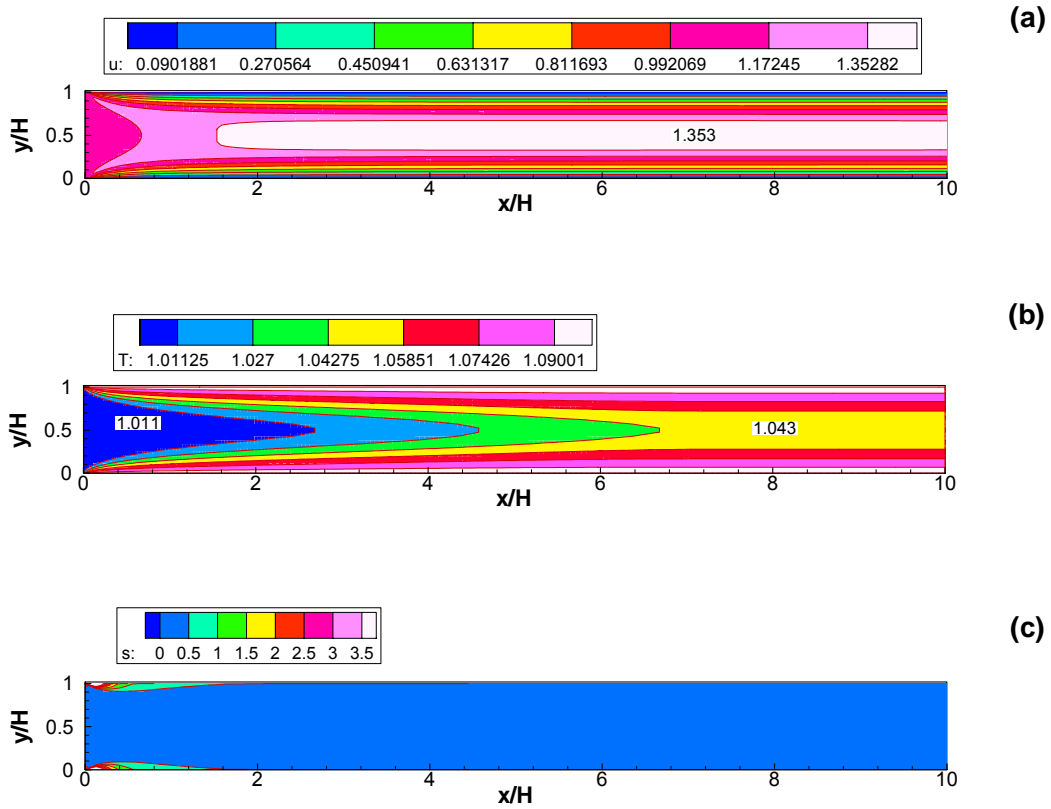**Figure 3. Nusselt number at the wall compared to solutions of Erbay et. al.[14]**

Figure 4. Contours of (a) *u*, (b) *T*, and (c) *s* for $T_w/T_\infty = 1.1$.

Figure 4 shows the *u*-velocity, temperature and entropy contours, which show good agreement with the plots presented by Erbay et. al[14] (not shown).

In order to determine the major contributions to entropy production, we have examined the following quantities from Eq. (3): $\dfrac{1}{\overline{T}}$, $\dfrac{1}{\overline{T}^2}$, $\dfrac{1}{\mathrm{Re}}\dfrac{1}{\overline{T}}\overline{\tau}_{ij}\dfrac{\partial \overline{u}_i}{\partial x_j}$, and $\dfrac{1}{(\gamma-1)M_\infty^2\,\mathrm{Re}\,\mathrm{Pr}}\dfrac{1}{\overline{T}^2}\left(\dfrac{\partial \overline{T}}{\partial x_j}\right)^2$. Figure 5 shows the relative values of these components. The calculations show that more than 90% of the entropy generation is due to viscous dissipation. This is consistent with the observations of Adeyinka and Naterer.[6] In general, most of the entropy is generated in the entry or inlet region or the developing region. This is due to the large velocity and temperature gradients that develop from the inlet prior to establishing a smooth temperature and velocity transition from the wall values.

(a)

(b)

(c)

(d)
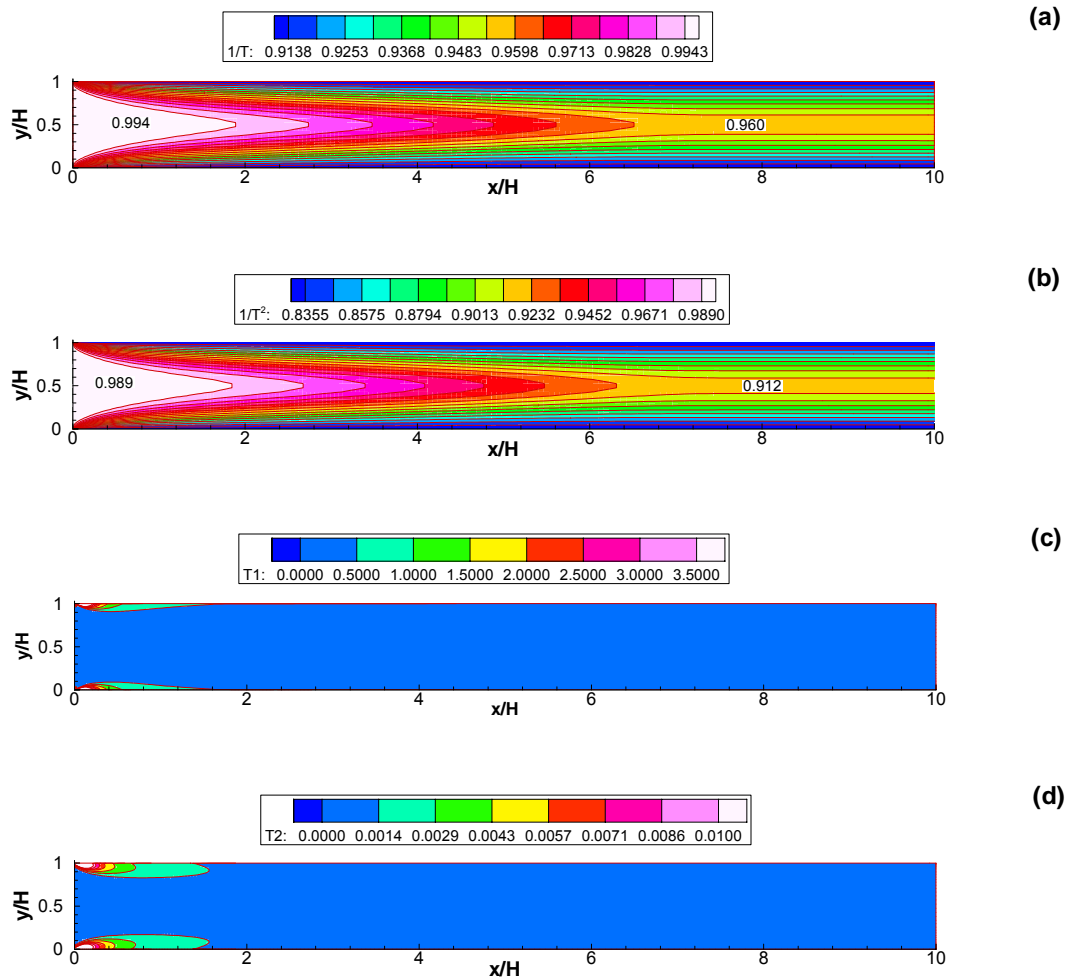
Figure 5. Contours of (a) $\dfrac{1}{\overline{T}}$, (b) $\dfrac{1}{\overline{T}^2}$, (c) $\dfrac{1}{\mathrm{Re}}\dfrac{1}{\overline{T}}\overline{\tau}_{ij}\dfrac{\partial \overline{u}_i}{\partial x_j}$, and (d) $\dfrac{1}{(\gamma-1)M_\infty^2\,\mathrm{Re}\,\mathrm{Pr}}\dfrac{1}{\overline{T}^2}\left(\dfrac{\partial \overline{T}}{\partial x_j}\right)^2$ for $T_w/T_\infty = 1.1$.

B. Turbulent Flow through a Channel

The turbulent channel flow calculation based is based on the same geometry as that reported in the last section, except that the grid used is 300 x 140 and the Reynolds number is in the range $7 \times 10^3 \le \text{Re} \le 50 \times 10^3$. In addition, the high-Reynolds number $k-\varepsilon$ turbulence model is used. This calculation is intended to validate the eddy viscosity model used for entropy calculations in the present paper. The entropy generation rate in the fully developed section of the channel is presented in Fig. 6. Adeyinka and Naterer[6] related the friction factor for a turbulent pipe flow to the entropy generation in the developed section using the following equation:

$$f = \frac{4}{\rho \bar{u}^3} \int \bar{T} \bar{\dot{S}}_{gen} dy . \tag{5}$$

Figure 6(b) shows the comparison of the current calculations using Eq. (5) with the Colebrook equation with good agreement.

(a)   (b)
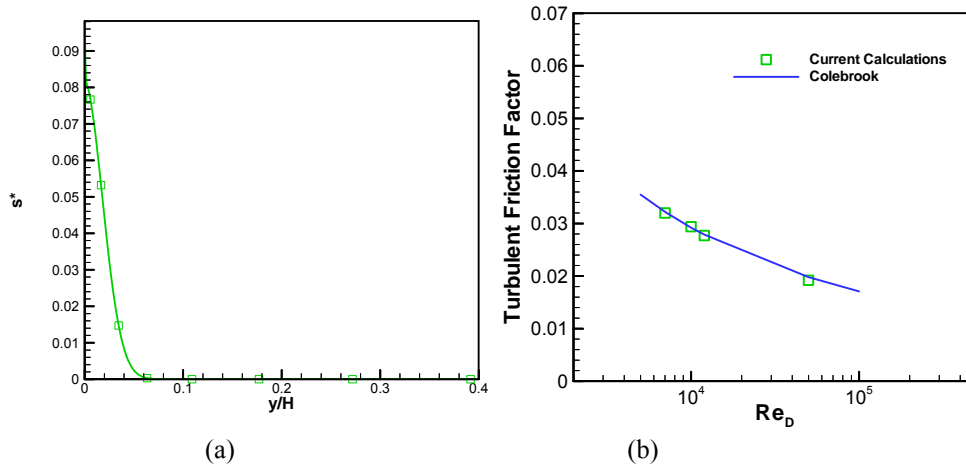
Figure 6. (a) Entropy distribution at *Re* = 10,000 and (b) friction factor compared with Colebrook equations for flow through a turbulent channel

C. Calculation of Flow over Boeing 747-200 Commercial Aircraft

The entropy production associated with the flow over a Boeing 747-200 commercial aircraft was calculated, as a way of generating exergy-based design data for the AFS-A subsystem of an integrated aircraft design/synthesis analysis. The following conditions were used: $M_\infty = 0.855$, $\alpha = 3.05^\circ$, reference area = 5500 sq ft (792,000 sq in), moment center = (1339.91, 0., 191.87) in., moment reference length = 327.8 in., and Re = 10680 per in. The spatial dimensions have been normalized with the moment reference length, leading to a reference Reynolds number, *Re* = *3.5×10⁶*. Both Euler and Navier-Stokes calculations were carried out using high-order discretization. The computational grids contained nine blocks with the following grid points: fuselage 138 x 70 x 30 = 416,000, nose cone 31 x 20 x 30 = 18,600, tail cap $(31 \times 20 \times 30 = 18,600)$, wing base 129 x 38 x 30 = 147,060, wing mid section 50 x 129 x 29 = 187,050, wing tip (top) 77 x 41 x 28 = 81,508, wing tip (bottom) 77 x 41 x 28 = 81,508, wing patch 71 x 71 x 71 = 357,911, and far-field grid 73 x 39 x 48 = 136,656. This yields a total number of grid points of 1,444,993. The first grid at the wall is located approximately at $\Delta y = 1 \times 10^{-4}$ which corresponds to a $y^+ \approx 80$. The grid used for the calculations is shown in Fig. 7 and described below.
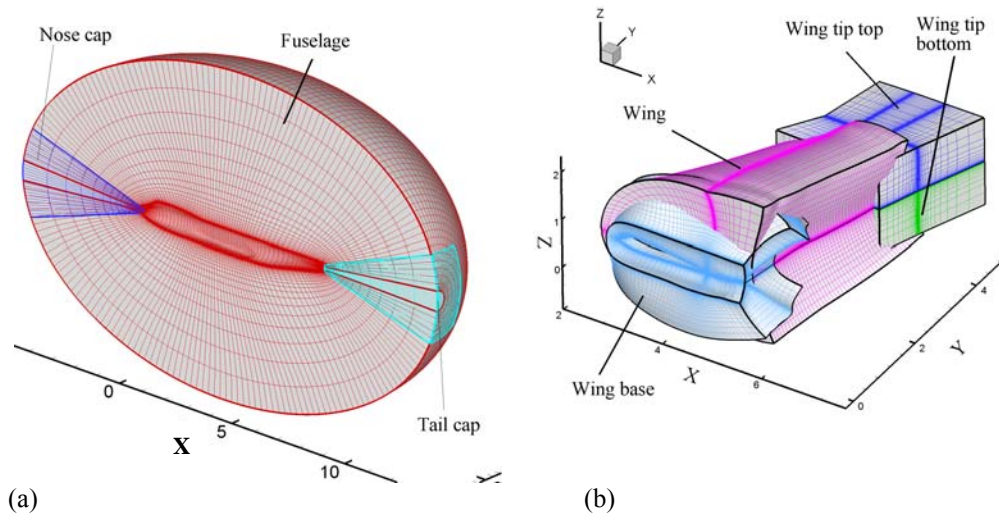
Figure 7. Mesh used for the computation of flow around the B747-200.

(a)   (b)

1. The B747-200 overset grid system

The fuselage surface is modeled using three overset blocks shown in Fig. 7(a). Block 2 (fuselage) spans most of the fuselage length in the physical *x*-direction. Blocks 3 and 4 are designed to cover the nose and tail surfaces of the fuselage. The later blocks are necessary to avert the computational singularities near the two poles.

Figure 7(b) shows an ensemble view of the computational grids, Blocks 5 through 8, around the wing. Block 5 (wing base) is a C-H type grid designed to connect the wing and fuselage surfaces. Block 6 (wing) is a C-type grid and extends over most of the wing span. Blocks 7 and 8 (wing tip top and bottom) consist of the H-H topology. The computational blocks around the wing exhibit enhanced grid density near the wing trailing edge and near the wing tip. For all computational blocks near solid walls (Blocks 2 through 8) the normalized grid space value at the wall is $\Delta = 1\times10^{-4}$.

A far-field box-shaped grid (not shown in Fig. 7) is designed to connect the computational blocks near the fuselage and the wing with far field conditions. For Block 1, the grids are clustered near the fuselage and wing blocks in all computational directions.

Details of the calculation and some of the difficulties encountered in performing the simulations are presented in a separate paper title.[18] The results are discussed below.

a)   b)
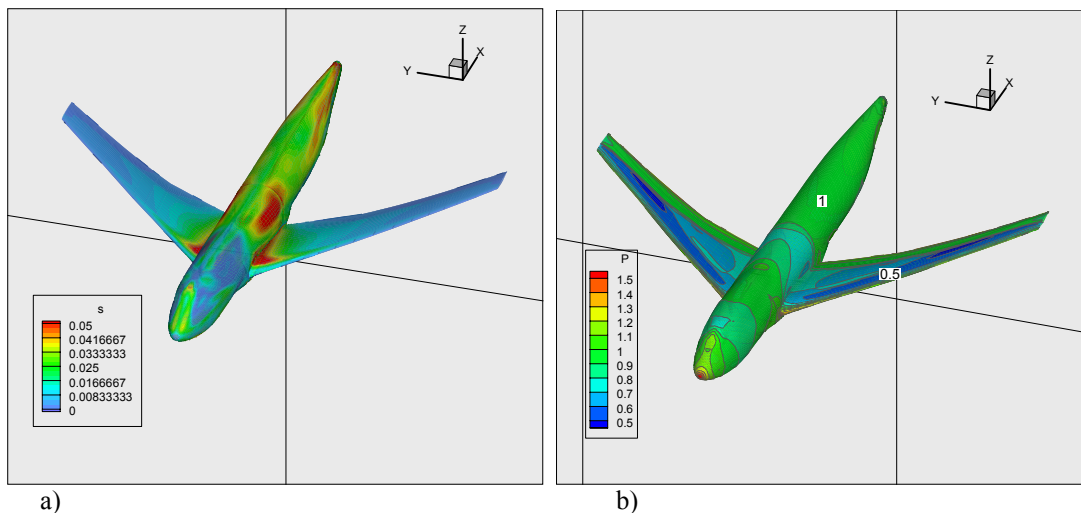
Figure 8. Contours of (a) entropy generation and (b) pressure around the B747-200 aircraft
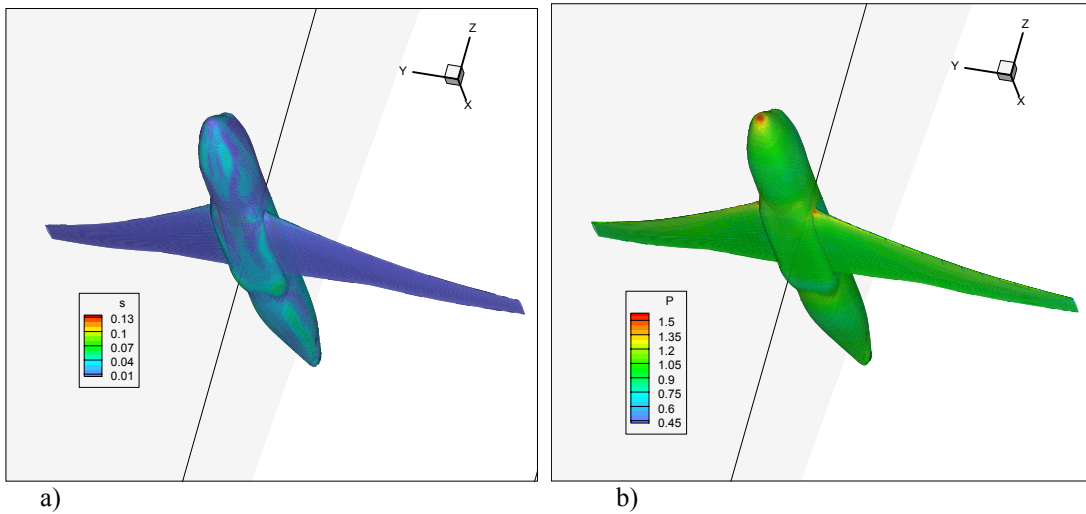
Figure 9. Contours of (a) entropy generation and (b) pressure around the bottom of the B747-200 aircraft
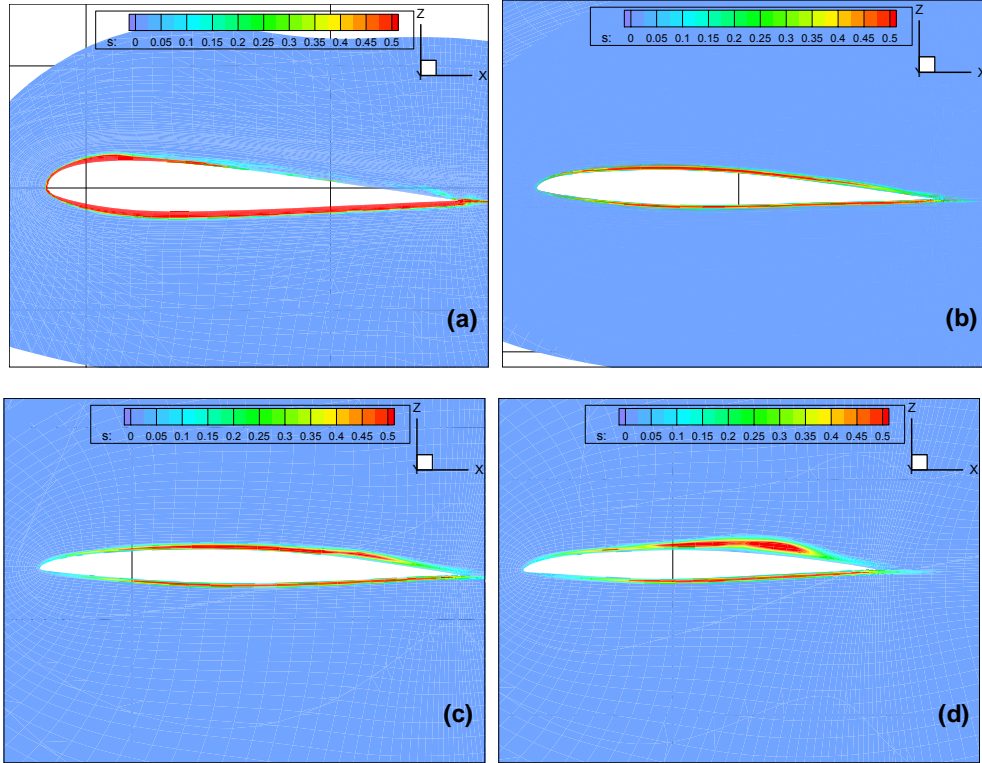
2. Viscous Entropy Generation

Figure 8 shows the entropy and pressure contours at the top of the fuselage and the suction side of the wing while Fig. 9 shows the analogous plots at the bottom of the fuselage and the pressure side of the wings, respectively. From these figures, it can be noted that much of the entropy at the surface is generated on the top part of the plane, in the nose region and in the tip of the wing where the velocity gradients are maximum. In addition, high entropy generation can be found on the fuselage just above the wings and on the wings close to the junction where the wings and fuselage meet.

Our calculations also show that most of the entropy is generated around the wing. This is illustrated in Figs. 10 and 11. Figure 10 shows the entropy generation around the fuselage. The figure shows very low values of entropy generation compared to those found around the wing in Fig. 11.
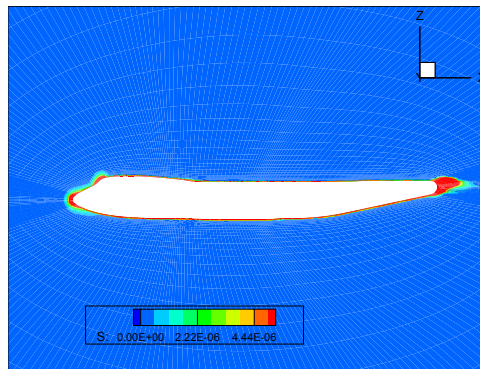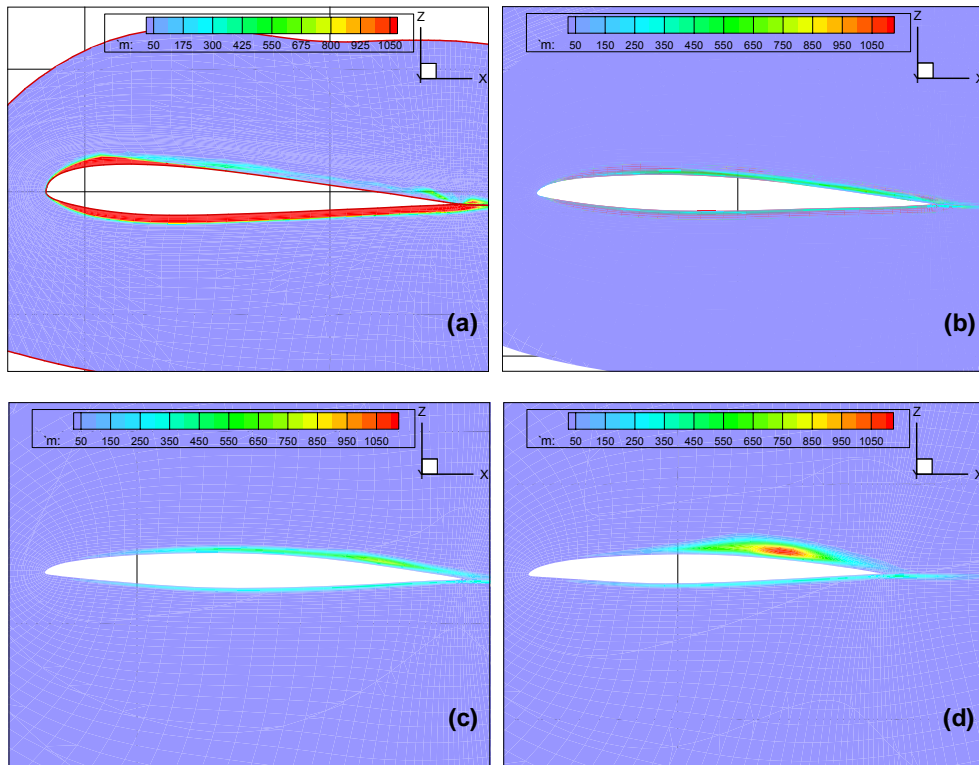

Figure 10. Viscous entropy generation around the fuselage

Figure 11. Viscous Entropy generation at wing locations: (a) 14%, (b) 28%, (c) 42%, and (d) 71%

Figure 12 shows the eddy viscosity plots at the same sections as in Fig. 11. The results show a correspondence between the areas of high eddy viscosity and entropy generation.

Figure 12 Eddy viscosities at various wing locations: (a) 14%, (b) 28%, (c) 42%, and (d) 71%

Figure 13 shows the relative contributions of the viscous dissipation-related term, $T1 \equiv \dfrac{1}{\mathrm{Re}} \dfrac{1}{\overline{T}} \overline{\tau}_{ij} \dfrac{\partial \overline{u}_i}{\partial x_j}$, and

$T2 \equiv \dfrac{1}{(\gamma-1)M_\infty^2 \, \mathrm{Re}\,\mathrm{Pr}} \dfrac{1}{\overline{T}^2}\left(\dfrac{\partial \overline{T}}{\partial x_j}\right)^2$, the heat transfer-related term (Eq. 3) to the entropy generation rate at 14% and

71% wing locations. The figures show that most of the entropy generation is due to viscous dissipation. However, closer to the fuselage (at the wing-fuselage junction), the heat transfer related term accounts for about 30% of the entropy generated and reduces to less than 5% further away from the fuselage. In the wing section from the base to about midpoint, the figure shows a high entropy generation close to the wing surface which reduces with the distance from the wing base. However, in the section between the midpoint and the wing tip, entropy generation increases on the suction side of the wing. In this section, there is provision for design improvement that will reduce the entropy generation rate on the suction side. In fact, as shown in Fig. 14, the high entropy generation on the suction side of the wing observable at 71% wing location also coincides with the separation region.

Figure 15 shows the temperature around the fuselage at 14% and 71% wing locations. A weak shock in the temperature profile that coincides with the locations of high entropy generation can be observed. This region has high temperature gradients and occurs around the slight separation bubble on the suction side of the wing. Figure 16

shows the plot of $1/\overline{T}$ while Fig.17 shows the plots of $\dfrac{1}{\mathrm{Re}} \dfrac{1}{\overline{T}} \overline{\tau}_{ij} \dfrac{\partial \overline{u}_i}{\partial x_j}$, and $\dfrac{1}{(\gamma-1)M_\infty^2 \, \mathrm{Re}\,\mathrm{Pr}} \dfrac{1}{\overline{T}^2}\left(\dfrac{\partial \overline{T}}{\partial x_j}\right)^2$. These figures

show that the gradient-related terms have larger contributions to entropy generation rate compared to $1/\overline{T}$ and $1/\overline{T}^2$.
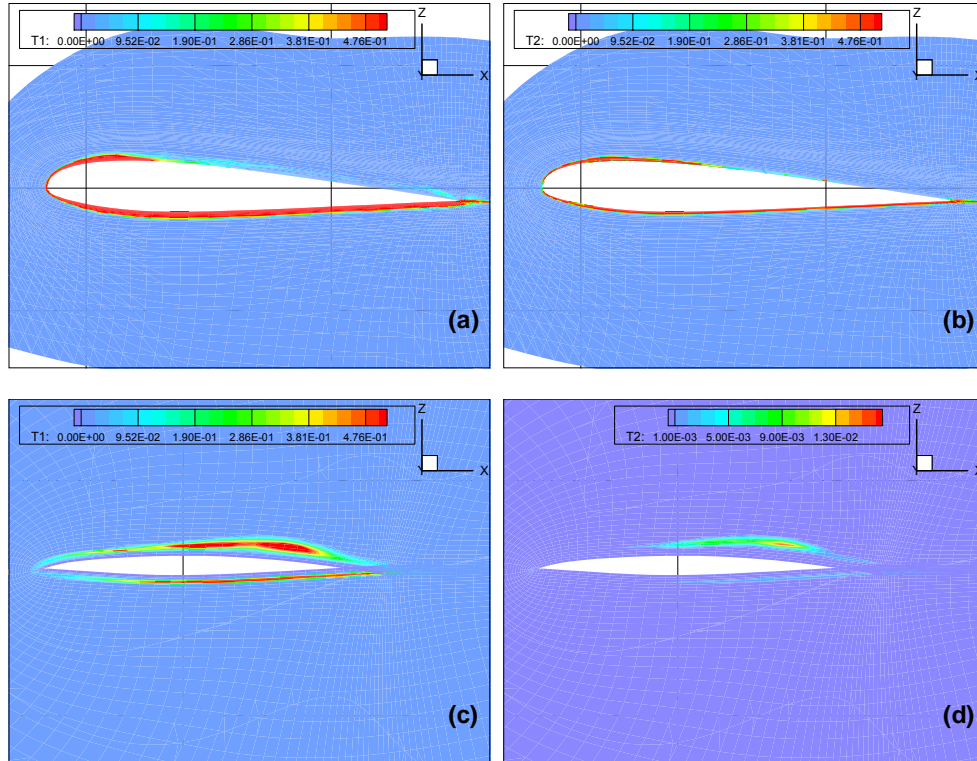
Figure 13 Entropy components $T1 \equiv \dfrac{1}{\mathrm{Re}} \dfrac{1}{\overline{T}} \overline{\tau}_{ij} \dfrac{\partial \overline{u}_i}{\partial x_j}$ **and** $T2 \equiv \dfrac{1}{(\gamma-1)M_\infty^2 \, \mathrm{Re}\,\mathrm{Pr}} \dfrac{1}{\overline{T}^2}\left(\dfrac{\partial \overline{T}}{\partial x_j}\right)^2$ **at 14% and 71% wing**

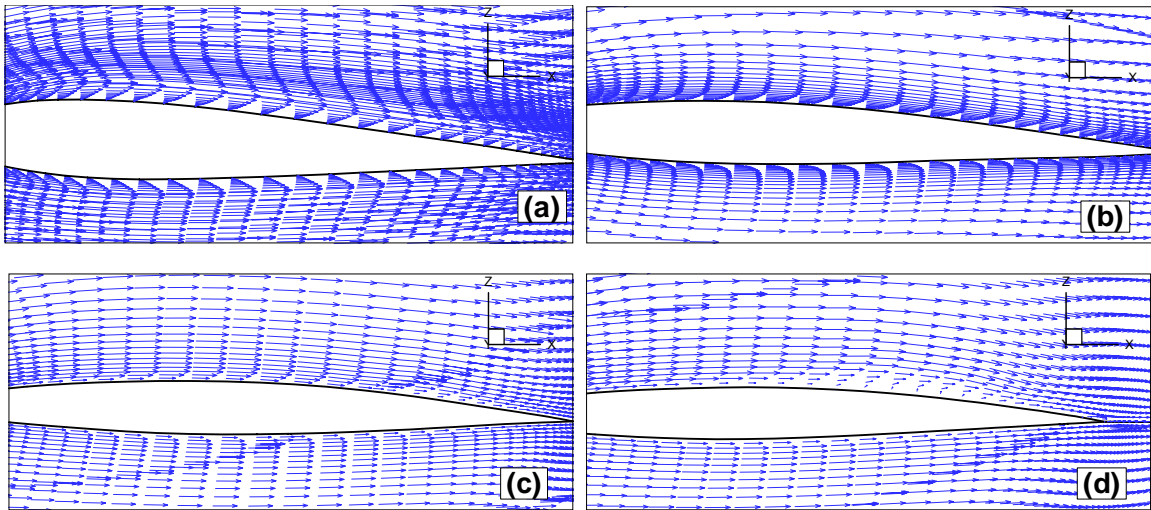**locations: (a) *T1* at 14%, (a) *T2* at 14%, (c) (a) *T1* at 71%, and (d) *T2* at 71%.**

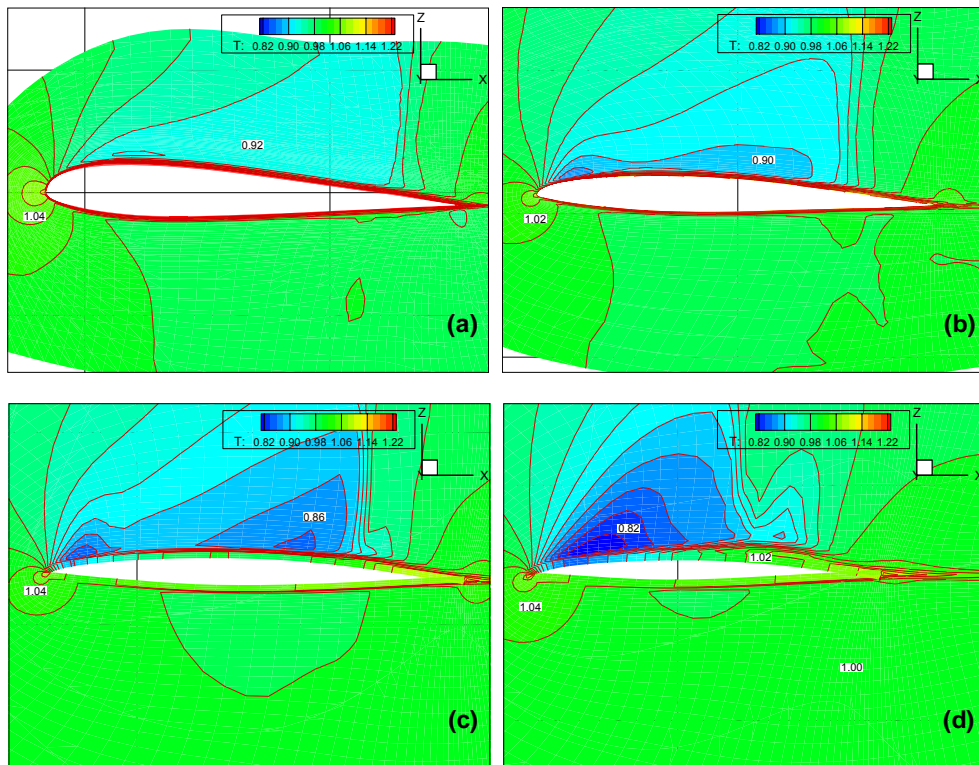**Figure 14 Velocity vectors at wing locations: (a) 14%, (b) 28%, (c) 42%, and (d) 71%**

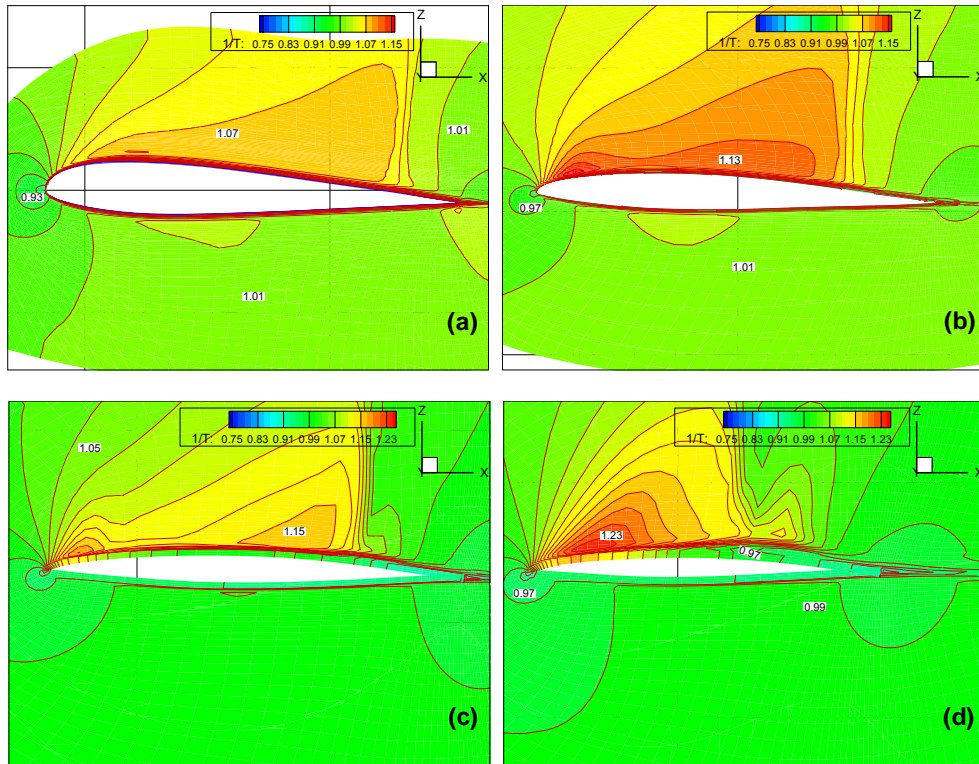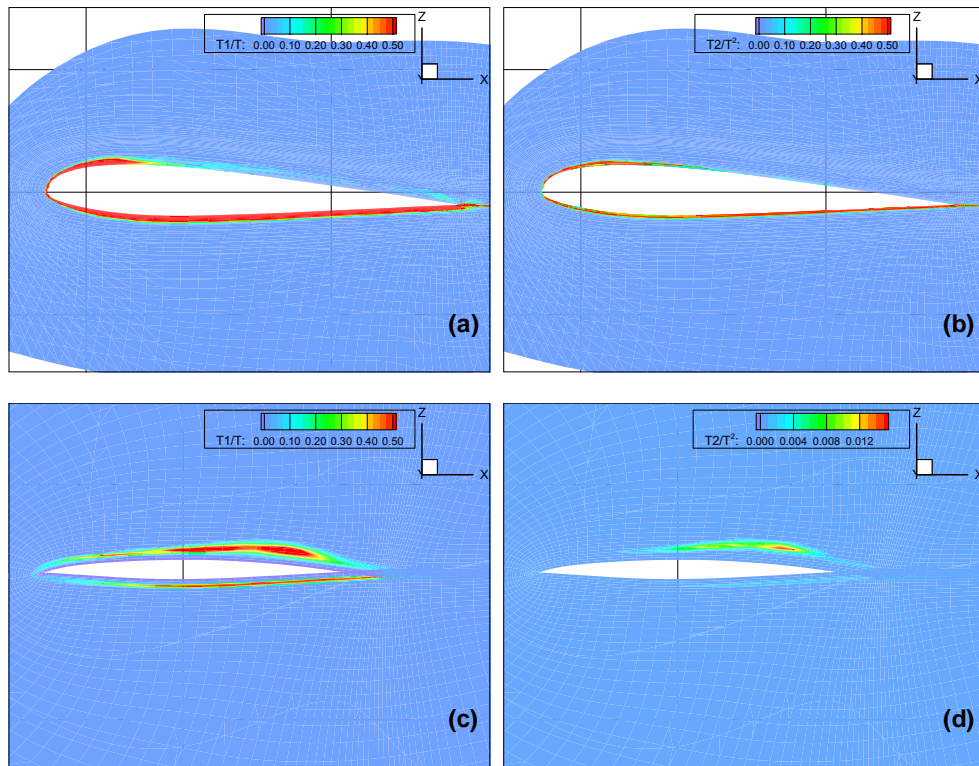**Figure 15 Temperature contours at wing locations: (a) 14%, (b) 28%, (c) 42%, and (d) 71%**

Figure 16 $1/\overline{T}$ **contours at wing locations: (a) 14%, (b) 28%, (c) 42%, and (d) 71%**

Figure 17 Entropy components $T1*\overline{T} \equiv \dfrac{1}{\mathrm{Re}}\,\overline{\tau}_{ij}\,\dfrac{\partial \overline{u}_i}{\partial x_j}$ **and** $T2*\overline{T}^2 \equiv \dfrac{1}{(\gamma-1)M_\infty^2\,\mathrm{Re}\,\mathrm{Pr}}\left(\dfrac{\partial \overline{T}}{\partial x_j}\right)^2$ **at 14% and 71% wing**

locations (a) *T1*T* **at 14%, (a)** *T2*T²* **at 14%, (c) (a)** *T1*T* **at 71%, and (d)** *T2* T²* **at** 71%.

3. Inviscid Entropy Generation

Figure 18 shows the entropy generation around the fuselage for the inviscid case, while Fig. 19 shows the entropy generation at several sections along the wing. The spikes in the entropy profile (Fig. 19) coincident with the shock locations on the wing can be noted when compared with the pressure contour of Fig. 8(b) and 20 which shows the coefficient of pressure for both viscous and inviscid calculations. In addition, the entropy generation persists in the wing wake region. The figures show that while the entropy generation around the fuselage was of the same scale for the viscous and inviscid calculations, the plots of entropy generation around the wing for the viscous calculations show entropy generation that is approximately 1000 times that of the inviscid calculations. Most of the entropy generated was located in the boundary layer. Considering the eddy viscosity plot in Fig. 12, it appears that the quantity, $(\mu + \mu_t)$, which has a magnitude of $\mu_t \approx 1000\mu$ accounts for the differences in the entropy production between both models.
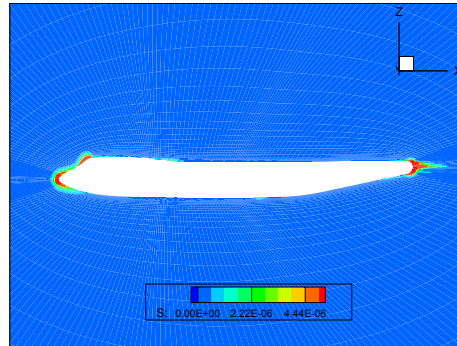

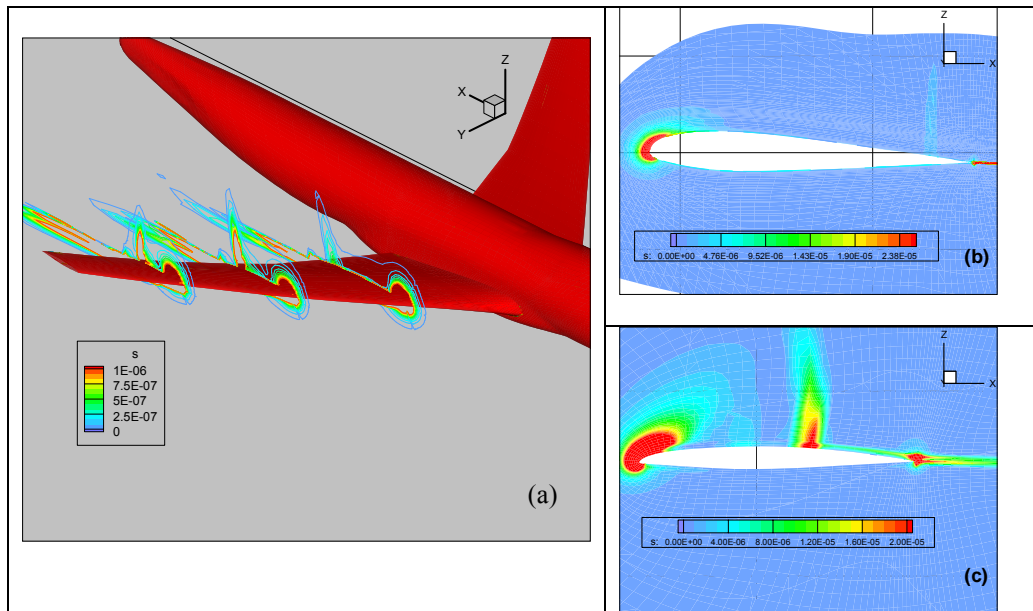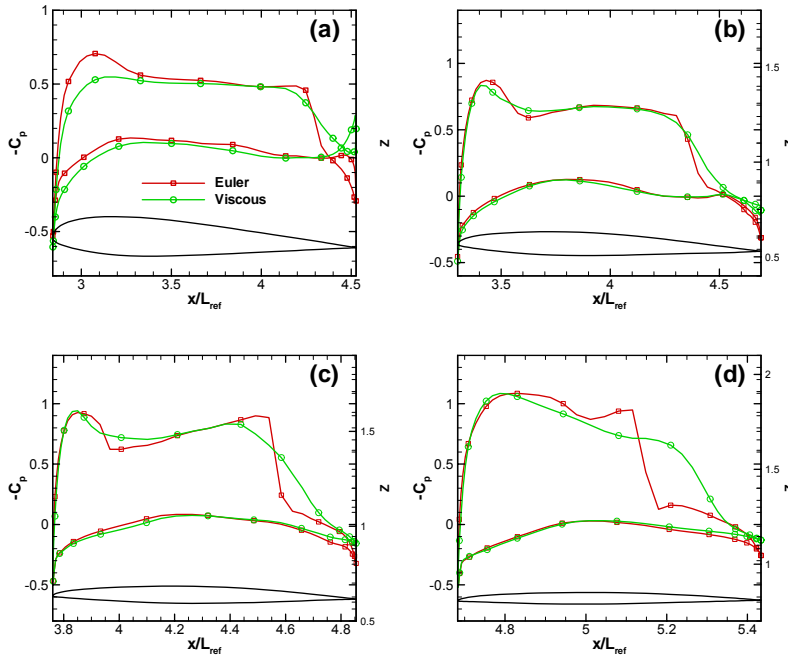**Figure 18. Inviscid entropy generation around the fuselage**

Figure 19. Inviscid entropy generation around the B747-200 wing (a) Several wing locations: (b) 14%, and (c) 71% wing locations

American Institute of Aeronautics and Astronautics

Figure 20 C_p profiles at wing locations: (a) 14%, (b) 28%, (c) 42%, and (d) 71%

Table 1 shows the total entropy integrated around the volume of the aircraft for viscous and inviscid calculations. The table shows the underestimation of entropy generation by inviscid models. This is expected on account of the neglect of the high velocity regions in the vicinity of the surfaces. In fact, most of the entropy generated in the inviscid calculations is found in the shock region.

Table 1. Total entropy generation by each block

Block	Inviscid	Viscous
1	2.06×10^{-6}	0.1044
2	8.70×10^{-8}	0.0014
3	2.66×10^{-7}	0.00042
4	4.95×10^{-3}	0.02656
5	4.93×10^{-6}	0.02722
6	8.53×10^{-7}	0.00313
7	3.642×10^{-7}	0.0029
8	5.306×10^{-7}	1.4×10^{-4}
9	$\sim 10^{-9}$	$\sim 10^{-9}$
Total	$\mathbf{4.96 \times 10^{-3}}$	**0.166**

IV.   Conclusion

The entropy generation around a B747-200 aircraft has been analyzed using computational fluid dynamics. The contributions of the various terms in the entropy equation were assessed. Viscous and inviscid models were investigated. The calculations show that inviscid results underestimate the total entropy production by a factor of about 1000 and only capture the entropy generation due to shock and at the stagnation and wake regions. A major difference between the two models was found to be due to the turbulent eddy viscosity present in the viscous calculations. Comparison of the entropy generation terms associated with the viscous calculations shows that the viscous dissipation contribute approximately 90% of the total entropy production term, with the heat transfer-related term contributing the remaining 10%. In addition, the calculations show possibility of design improvement particularly in the wing sections removed away from the fuselage.

Acknowledgments

References

[1]Rancruel, D. F., A Decomposition Strategy Based on Thermoeconomic Isolation Applied to the Optimal Synthesis/Design and Operation of an Advanced Fighter Aircraft System, M.Sc. Thesis, Virginia State University, 2002.

[2]Rancruel, D. F., von Spakovsky, M. R., 2004, Use of a Unique Decomposition Strategy for the Optimal Synthesis/Design and Operation of an Advanced Fighter Aircraft System, 10th AIAA/ISSMO Multi- disciplinary Analysis and Optimization Conference, Aug. 30 - Sept. 1, Albany, New York.

[3]Muñoz, J.R., von Spakovsky, M.R., 2003, Decomposition in Energy System Synthesis / Design Optimization for Stationary and Aerospace Applications, AIAA Journal of Aircraft, special issue, Vol. 39, No. 6, Jan-Feb.

4Adeyinka, O. B. and Naterer, G. F., "Predicted Entropy and Measures with Particle Image Velocimetry" AIAA 2002-2090, 2002.

[5]Sciubba, E., "Calculating Entropy with CFD" Mech, Eng (ASME) 119(10), 1997, pp 86-88.

[6]Adeyinka, O. B. and Naterer, G. F., "Modeling of Entropy Production in Turbulent Flows" J. Fluid Eng. Vol. 126, 2004.pp. 893-899.

[7]Naterer, G. F., and Camberos, J. A., "Entropy Production Rates from Viscous Flow Calculations" . J. Thermophys. & Heat Transfer 17(3), 2003, pp 360-371.

[8]Kramer-Bevan, J. S., "A tool for Analysis of Fluid Flow Losses" M.Sc Thesis, University of Waterloo, Canada,1992,.

[9]Bejan, A., "Entropy Generation Minimization: The Method of Thermodynamic Optimization of Finite-Time Systems and Finite-Time Processes", CRC Press. New York 1996.

[10]Moore, J., and Moore, J. G., 1983. "Entropy Production Rates from Viscous Flow Calculations, Part I. A Turbulent Boundary Layer Flow," ASME Paper 83-GT-70, ASME Gas Turbine Conference, Phoenix, AZ.

[11]F. Kock, H. Herwig: Local Entropy Production in Turbulent Shear Flows: A High Reynolds Number Model with Wall functions, erscheint in: Int. J. Heat Mass Transfer, 2004

[12]Thaerocomp Technical Corp. "AEROFLO User's Manual", 2004.

[13]Erbay, L. B., Ercan, M. S., Sulus, B., and Yalcin, M. M., 2003. "Entropy Generation During Fluid Flow Between Two Parallel Plates with Moving Bottom Plate", Entropy, 5, 506-518.

[14]Sahin, A. Z., "Entropy Generation in a Turbulent Liquid Fluid Flow Through a Smooth Duct Subjected to Constant Wall Temperature", Int. Journal of Heat and Mass Transfer, vol. 43, pp. 1469-1478, 2000.

[15]Kakac, S. and Yener, Y., 1995. "Convective Heat Transfer", CRC Press, 2nd ed.

[16]Mahmud,S., Fraser, R. A., "Thermodynamic Analysis of Flow and Heat Transfer Inside Channel with Two Parallel Plates", Exergy, an International Journal, vol. 2, pp. 140-146, 2002.

[17]Steffen, C. J., "A Critical Comparison of Several Low Reynolds Number k-ε Turbulence Models for Flow Over a Backward-Facing Step", NASA Technical Memorandum 106173. AIAA-93-1927.

[18]Ladeinde, F., Alabi, K., Safta, C., Cai, X., 2006. "The First High –Order Simulation of Aircraft: Challenges and Opportunities", AIAA 2006-1526. 44th Aerospace Sciences Meeting, Reno, NV, January 2006.

[19]Jameson, A., 2003. "CFD for Aerodynamic Design and Optimization: Its Evolution over the Last Three Decades", AIAA 2003-3438.